Two-dimensional Green's tensor for gyrotropic clusters composed of circular cylinders

Ara A. Asatryan,[1,*] Lindsay C. Botten,[2] Kejie Fang,[3] Shanhui Fan,[3] and Ross C. McPhedran[4]

[1]*School of Mathematical Sciences, University of Technology Sydney, Sydney, NSW 2007, Australia*
[2]*School of Mathematical Sciences and Centre for Ultrahigh-bandwidth Devices for Optical Systems (CUDOS), University of Technology Sydney, Sydney, NSW 2007, Australia*
[3]*Department of Electrical Engineering, Stanford University, Stanford, California 94305, USA*
[4]*School of Physics and CUDOS, University of Sydney, Sydney, NSW 2006, Australia*
**Corresponding author: ara.asatrian@uts.edu.au*

Received July 1, 2014; accepted August 25, 2014;
posted September 3, 2014 (Doc. ID 214986); published September 26, 2014

The construction of Green's tensor for two-dimensional gyrotropic photonic clusters composed of cylinders with circular cross sections using the semi-analytic multipole method is presented. The high efficiency and accuracy of the method is demonstrated. The developed method is applied to gyrotropic clusters that support topological chiral Hall edge states. The remarkable tolerance of chiral Hall edge modes toward substantial cluster separation is revealed. The transformation of chiral Hall edge states as the cluster separation increases is also presented. The excitation of chiral Hall edge modes for different source orientations is considered. Both gyroelectric and gyromagnetic (ferrite) clusters are treated. © 2014 Optical Society of America

OCIS codes: (290.5825) Scattering theory; (160.1585) Chiral media; (050.5298) Photonic crystals.
http://dx.doi.org/10.1364/JOSAA.31.002294

1. INTRODUCTION

The subject of topological photonics has attracted substantial attention recently [1–8]. This interest was sparked by the highly influential papers of Haldane and Raghu [9,10] in which the existence of the direct photonic analog of topological chiral Hall edge states was established. A necessary condition for the existence of such photonic topological states is the breaking of time reversal symmetry [11], which can be achieved, for example, in gyrotropic media.

Such strong interest in the properties of photonic chiral Hall edge states is based on two of their intrinsic properties—*immunity to both disorder and backscattering*. Both of these properties can be utilized to construct highly efficient nanoscale nonreciprocal devices, such as one-way waveguides [1], optical isolators, and buffers.

The topological chiral Hall edge states exist at the interface of two photonic crystals that have bands with different topological Chern numbers [1–3,8–10]. The Chern number of bands can take only integer values and is nonzero only when the time-reversal invariance is broken. The immunity to disorder of chiral Hall edge states originates from the fact that moderate disorder cannot change the value of an integer Chern number, leading to the preservation of waveguide guiding properties. Note that the quantized Hall conductance is proportional to this Chern number [12].

Backscattering in such structures is forbidden given that there is no backward mode associated to the forward propagating mode due to time-reversal breaking. Although embedded waveguides in photonic crystals are tolerant toward mild disorder [13,14], the waveguides embedded in topological photonic crystals are far more robust to disorder due to their topological protection.

Initial research has been focused on the design of photonic structures that can support topological states [1–10]. The excitation of such states may require the presence of internal sources. Therefore, knowledge of the radiation properties of sources embedded in such structures is also important. These radiation properties are determined by the optical local density of states (LDOS), which can be deduced from the imaginary part of the trace of the electromagnetic Green's tensor [15,16].

In a recent paper [17], the Green's tensor was constructed for two-dimensional gyrotropic clusters composed of cylinders with circular cross sections based on the multipole method. The LDOS of gyrotropic clusters that support the topological chiral Hall edge states were characterized also. However, details of the Green's tensor construction have not yet been given. Therefore, a principal purpose of this paper is to provide details of the construction of the Green's tensor for a cluster composed of gyrotropic two-dimensional cylinders and to show the efficiency and accuracy of this method.

The developed method has been applied to investigate chiral Hall edge state properties and their excitations for both gyroelectric and ferrite clusters. For ferrite clusters, we consider the tolerance of chiral Hall edge states toward cluster separation, in which we split the initial cluster into two approximately equal parts and displace them. We also investigate the transformation properties of the chiral Hall edge states as the cluster separation changes. For a gyroelectric cluster, we present the results of the chiral Hall edge state excitation for different source orientations. The calculation of the spatial profiles of chiral Hall edge states, their quality factors, and their energy flow maps are also presented.

 © 2014 Optical Society of America

In Section 2 we provide details of the Green's tensor construction of gyrotropic photonic clusters based on the multipole approach. The calculation of modal profiles of such clusters is also provided. In Section 3 we present details of convergence studies and numerical verification of results. In Section 4 we investigate the tolerance and the transformation properties of chiral Hall edge states as a function of the cluster separation. The excitations of chiral Hall edge states for different source orientations is also presented.

2. THEORETICAL TREATMENT

In this section we provide details of the Green's tensor construction based on the multipole method for two-dimensional ferrite and gyroelectric photonic clusters composed of cylinders with circular cross sections. The method can also be applied to calculate the chiral Hall edge mode profiles, their quality factors, and their energy flow maps. The multipole method has been proven to be an efficient and accurate method for the Green's tensor calculation for the case of scalar material equations [18–20]. Here we show that the multipole method is effective also for anisotropic materials.

The problem's geometry is depicted in Fig. 1. The cluster consists of N_c nonoverlapping cylinders with infinite length oriented along the z axis with radii a_l, centered at positions $\mathbf{c}_l$ in the x–y plane. For this two-dimensional geometry, the polarizations are decoupled and the field for ferrite clusters is determined by a single component E_z for TM polarization, and it is specified by the H_z component for TE polarization and gyroelectric cylinders. The solution for TE polarization for ferrite cylinders and the TM polarization for gyroelectric cylinders can be reduced to the known scalar cases presented in [18]. Thus, for ferrite clusters, we consider only TM polarization, and for the gyroelectric cylinders we consider only TE polarization.

The time dependence we choose in the form $e^{-i\omega t}$, and we scale the magnetic field by the free-space impedance Z_0, $Z_0\mathbf{H} \to \mathbf{H}$. The external static magnetic field $\mathbf{H}_0$ is applied along the z axis and provides the material with gyrotropic properties.

A. Green's Function for Ferrite Clusters

The ferrite cylinders have a scalar dielectric permittivity ε_l and a dispersive tensorial magnetic permeability $\hat{\mu}_l(\omega)$ given by [21]

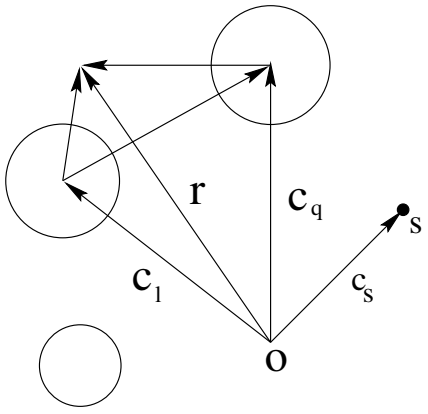

Fig. 1. x–y cross section of a gyrotropic cluster.

$$\hat{\mu}_l(\omega) = \begin{pmatrix} \mu_{\perp,l} & i\mu_{xy,l} & 0 \\ -i\mu_{xy,l} & \mu_{\perp,l} & 0 \\ 0 & 0 & \mu_{\parallel,l} \end{pmatrix}. \tag{1}$$

The cylinders are located in a ferrite background medium with a dielectric permittivity ε_b and a magnetic permeability tensor $\hat{\mu}_b(\omega)$, which has a similar form to that in Eq. (1).

From Maxwell's equations it can be shown that, for this two-dimensional geometry, Green's tensor $\mathbf{G}^e$ for TM polarization reduces to a form involving only a single scalar E_z, which satisfies the following equation:

$$\nabla^2 E_z(\mathbf{r};\mathbf{c}_s) + k^2 n^2(\mathbf{r}) E_z(\mathbf{r};\mathbf{c}_s) = -\delta(\mathbf{r}-\mathbf{c}_s), \tag{2}$$

where $n^2(\mathbf{r}) = \varepsilon(\mu_\perp^2 - \mu_{xy}^2)/\mu_\perp$ takes the role of either the refractive index of the lth cylinder $n_l(\mathbf{r})$ or the refractive index of the background n_b.

The corresponding magnetic field components can be found from the Maxwell equation $\mathbf{H} = \hat{\mu}^{-1}\nabla \times \mathbf{E}/ik$. Equation (2) needs to be solved subject to the boundary conditions requiring the continuity of the tangential fields E_z and H_θ at the boundary of all cylinders. The calculation of the spatial profiles of chiral Hall edge states is also constructed from the solution of Eq. (2), but without the right-hand-side source term.

Finding the solution of this problem is quite similar to the scalar case [18] and the only difference is associated with the boundary conditions. We represent the exterior field in the background medium at the vicinity of the lth cylinder with local coordinates $\mathbf{r}_l = (r_l, \theta_l) = \mathbf{r} - \mathbf{c}_l$ in the form

$$E_z = \sum_{m=-\infty}^{\infty} [A_m^l J_m(kn_b r_l) + B_m^l H_m^{(1)}(kn_b r_l)] e^{im\theta_l}. \tag{3}$$

This local expansion is valid in the annular region centered at the center of cylinder l and spans between the surface of cylinder l to the nearest cylinder or source. The multipole coefficients $\mathbf{A}^l = [A_m^l]$ represent the local field in the vicinity of the lth cylinder originating from all other cylinders or external sources and $\mathbf{B}^l = [B_m^l]$ represents the outgoing field of the lth cylinder. The field expansion, which is valid at every exterior point, can be expressed in the form

$$E_z(\mathbf{r};\mathbf{c}_s) = \frac{1}{4i} H_0^{(1)}(kn_b|\mathbf{r}-\mathbf{c}_s|) + \sum_{l=1}^{N_c} \sum_{m=-\infty}^{\infty} B_m^l H_m^{(1)}(kn_b|\mathbf{r}_l|) e^{im\,\arg(\mathbf{r}_l)}, \tag{4}$$

where $\mathbf{r}_l = \mathbf{r} - \mathbf{c}_l$. The first term in Eq. (4) is absent if the source is located inside of one of the cylinders. For the derivation of this global expansion, see [18].

We apply Graf's addition theorem for Bessel functions [22] to Eq. (4), and express the global expansion in the local coordinate system of the lth cylinder. Then we equate the obtained relation to the local expansion of Eq. (3) and deduce the field identity

$$A_m^l = K_m^l + \sum_{q=1, q\neq l}^{N_c} \sum_{p=-\infty}^{\infty} S_{mp}^{lq} B_p^q, \tag{5}$$

where

$$K_m^l = \frac{1}{4i} H_m^{(1)}(kn_b c_{ls}) e^{-im\theta_{ls}}, \tag{6}$$

$$S_{mp}^{lq} = H_{m-p}^{(1)}(kn_b c_{lq}) e^{i(p-m)\theta_{lq}}. \tag{7}$$

Here, (c_{lq}, θ_{lq}) are the local polar coordinates of $\mathbf{c}_{lq} = \mathbf{c}_q - \mathbf{c}_l$, the position of cylinder q relative to cylinder l, and, correspondingly, (c_{ls}, θ_{ls}) are the local polar coordinates of $\mathbf{c}_{ls} = \mathbf{c}_s - \mathbf{c}_l$, the position of the source s relative to cylinder l. The obtained field identity of Eq. (5) can be expressed in matrix form:

$$\mathbf{A} = \mathbf{SB} + \mathbf{K}, \tag{8}$$

where the vectors $\mathbf{A} = [\mathbf{A}^l]$, $\mathbf{B} = [\mathbf{B}^l]$, $\mathbf{K} = [\mathbf{K}^l]$ are partitioned vectors of the multipole coefficients associated with the lth cylinder and matrix $\mathbf{S}$ is $\mathbf{S} = [\mathbf{S}^{lq}]$, where $[\mathbf{S}^{lq}] = S_{mp}^{lq}$.

The interior field expansion for the lth cylinder can be expressed as

$$E_z(\mathbf{r}; \mathbf{c}_s) = \frac{1}{4i} H_0^{(1)}(kn_l|\mathbf{r} - \mathbf{c}_s|) + \sum_{m=-\infty}^{\infty} C_m^l J_m(kn_l|\mathbf{r}_l|) e^{im \arg(\mathbf{r}_l)}, \tag{9}$$

where the first term is the source term. After application of Graf's addition theorem to the first term in Eq. (9), we deduce

$$E_z(\mathbf{r}; \mathbf{c}_s) = \sum_{m=-\infty}^{\infty} Q_m^l H_m^{(1)}(kn_l r_l) e^{im\theta_l} + \sum_{m=-\infty}^{\infty} C_m^l J_m(kn_l r_l) e^{im\theta_l}, \tag{10}$$

where

$$Q_m^l = \frac{1}{4i} J_m(kn_l c_{ls}) e^{-im\theta_{ls}} \tag{11}$$

denotes the multipole coefficients of an interior source s in the local coordinates of cylinder l and $(c_{ls}, \theta_{ls}) = \mathbf{c}_{ls} = \mathbf{c}_s - \mathbf{c}_l$, If the source is located in the background then the source term is absent in Eq. (9).

Using the exterior [Eq. (3)] and the interior [Eq. (10)] field expansions and the field tangential components E_z and H_θ continuity conditions, we deduce

$$B_m^l = R_m^l A_m^l + T_m^l Q_m^l, \tag{12}$$

$$C_m^l = R_m'^l A_m^l + T_m'^l Q_m^l, \tag{13}$$

where the exterior field $\{A_m^l\}$ and the interior $\{Q_m^l\}$ fields can be regarded as "incoming" fields to the boundary of cylinder l, generating the exterior $\{B_m^l\}$ and interior $\{C_m^l\}$ fields. The explicit expressions of the cylinder interface transmission and reflection coefficients are given in Appendix A [see Eqs (A1)–(A4) and (A6)–(A9)]. In matrix form, Eqs. (12) and (13) become

$$\mathbf{B} = \mathbf{RA} + \mathbf{TQ}, \tag{14}$$

$$\mathbf{C} = \mathbf{T}'\mathbf{A} + \mathbf{R}'\mathbf{Q}, \tag{15}$$

where $\mathbf{R} = \mathrm{diag}\mathbf{R}^l$ is a diagonal matrix of diagonal matrices $\mathbf{R}^l = \mathrm{diag}R_m^l$, and with similar definitions applying for the other reflection and transmission matrices. Now the substitution of $\mathbf{A}$ from Eq. (8) into Eq. (14) leads to the infinite linear system of equations

$$(\mathbf{I} - \mathbf{RS})\mathbf{B} = \mathbf{RK} + \mathbf{TQ}. \tag{16}$$

For any exterior source, the $\mathbf{K}^q$ are nontrivial for all q, while for a source within cylinder l, the $\mathbf{Q}^q$ for $q \neq l$ are trivial and only $\mathbf{Q}^l$ is nonzero. Only the exterior source $\mathbf{K}$ or interior source Q are taken to be present at the one time in Eq. (16).

Equation (16) is an infinite-dimensional linear system and needs to be truncated in its numerical implementation. The truncation parameter is given by the number of retained multipole coefficients per cylinder, $N_p = 2M + 1$, where M denotes the largest retained multipole order. The accuracy of the solution is determined by N_p representing the number of multipole coefficients. After finding the external multipole coefficients $\mathbf{B}$ from Eq. (16), the internal coefficients $\mathbf{C}$ can be found from the boundary condition of Eq. (15).

Note that the nonreciprocal behavior of the considered clusters originates from the boundary conditions. The presence of the δ_m terms in Eqs. (A1)–(A4) from Appendix A breaks the rotational symmetries of the cylinder's reflection and transmission coefficients $R_{-m}^l \neq R_m^l$, $T_{-m}^l \neq T_m^l$. Under certain conditions, this symmetry breaking can be unidirectional for all cylinders in the cluster, leading to chiral behavior. The external E_z field can be reconstructed from the global expansion [Eq. (4)], while the internal field of the lth cylinder can be calculated using the local expansion [Eq. (9)]. The magnetic field components then can be calculated using Maxwell's equations.

B. Green's Tensor for Gyroelectric Clusters

In this section we provide details of the Green's tensor construction for gyroelectric clusters. The cluster is composed of gyroelectric cylinders with material parameters $\hat{\varepsilon}_l(\omega)$ and $\mu_l(\omega)$, where the dielectric permittivity $\hat{\varepsilon}_l(\omega)$ is a tensor, while the magnetic permeability $\mu_l(\omega)$ is a scalar. The cylinders are located in a gyroelectric background medium with material parameters $\hat{\varepsilon}_b(\omega)$ and $\mu_b(\omega)$. The dielectric permittivity tensor of a gyroelectric material has the form

$$\hat{\varepsilon} = \begin{pmatrix} \varepsilon_\perp & i\varepsilon_{xy} & 0 \\ -i\varepsilon_{xy} & \varepsilon_\perp & 0 \\ 0 & 0 & \varepsilon_\parallel \end{pmatrix}, \tag{17}$$

where we have assumed that the external static magnetic field is aligned along the z axis. The positions of the cylinders, their radii, and their material characteristics can be arbitrary.

For TE polarization, the electromagnetic field is characterized by only the H_z component, which is given by the solution of the equation

$$(\nabla^2 + k^2 n^2(\mathbf{r})) H_z(\mathbf{r}) = i\hat{\mathbf{z}} \cdot [\nabla \times (\hat{\varepsilon}^{-1}\mathbf{u}\delta(\mathbf{r} - \mathbf{c}_s))]/k, \tag{18}$$

where $n^2(\mathbf{r}) = \mu(\varepsilon_\perp^2 - \varepsilon_{xy}^2)/\varepsilon_\perp$ and $\hat{\varepsilon}^{-1}$ is the inverse of the dielectric tensor [Eq. (17)]. To find all the components of the

electric Green's tensor $\mathbf{G}^e$, it is necessary to solve Eq. (18) for two source orientations $\mathbf{u} = \mathbf{x}, \mathbf{y}$ and find the corresponding electric field components from the Maxwell equation $\mathbf{E} = -\hat{\varepsilon}^{-1}\nabla \times \mathbf{H}/ik$. The electric Green's tensor reduces to a 2×2 tensor:

$$\mathbf{G}^e = \begin{pmatrix} G_{xx} & G_{xy} & 0 \\ G_{yx} & G_{yy} & 0 \\ 0 & 0 & 0 \end{pmatrix}. \tag{19}$$

The magnetic field H_z in the background can be expressed in the form

$$H_z = H_z^{0u} + \sum_{l=1}^{N_c} \sum_{m=-\infty}^{\infty} B_m^l H_m^{(1)}(kn_b|\mathbf{r} - \mathbf{c}_l|)e^{im\ \arg(\mathbf{r}-\mathbf{c}_l)}, \tag{20}$$

where the first term is the magnetic field of a dipole source in a homogeneous gyroelectric medium with source orientations $u = \hat{x}, \hat{y}$. The explicit forms of these are given by

$$H_z^{0x} = \frac{n_b}{4}\left(\sin\theta - \frac{i\varepsilon_{xy,b}}{\varepsilon_{\perp,b}}\cos\theta\right)H_1^{(1)}(kn_b|\mathbf{r}_s|), \tag{21}$$

$$H_z^{0y} = -\frac{n_b}{4}\left(\cos\theta + \frac{i\varepsilon_{xy,b}}{\varepsilon_{\perp,b}}\sin\theta\right)H_1^{(1)}(kn_b|\mathbf{r}_s|), \tag{22}$$

where $|\mathbf{r}_s| = |\mathbf{r} - \mathbf{c}_s|$ and $\theta = \arg(\mathbf{r} - \mathbf{c}_s)$. The corresponding interior expansion is

$$H_z = H_z^{0u} + \sum_{m=-\infty}^{\infty} C_m^l J_m(kn_l|\mathbf{r} - \mathbf{c}_l|)e^{im\ \arg(\mathbf{r}-\mathbf{c}_l)}, \tag{23}$$

where H_z^{0u} has the same form as Eqs. (21) and (22), but n_b, $\varepsilon_{\perp,b}$ and $\varepsilon_{xy,b}$ are replaced with the corresponding values for the lth cylinder.

To construct the components of the Green's tensor, it is necessary to solve two scattering problems associated with the dipole sources given by Eqs. (21) and (22). The derivation of the linear system is similar to that for the E_z polarization. The coefficient matrix $\mathbf{I} - \mathbf{RS}$, on the left-hand side of Eq. (16), has precisely the same form, with the exception that the reflection matrix $\mathbf{R}$ is replaced by its H_z polarization form, which is given in Appendix A. The main difference occurs in the exterior and interior source vectors $\mathbf{K}$ and $\mathbf{Q}$, which now contain coefficients for the cylindrical harmonic expansions of the dipole source term H_z^{0u}. For the dipole source term H_z^{0x}, the $\mathbf{K}$ and $\mathbf{Q}$ are given by

$$K_m^l = -\frac{n_b}{8i}\left[\left(1 + \frac{\varepsilon_{xy,b}}{\varepsilon_{\perp,b}}\right)H_{m-1}(kn_b r_{ls})e^{-i(m-1)\theta_{ls}} + \left(1 - \frac{\varepsilon_{xy,b}}{\varepsilon_{\perp,b}}\right)H_{m+1}(kn_b r_{ls})e^{-i(m+1)\theta_{ls}}\right], \tag{24}$$

$$Q_m^l = \frac{n_l}{8i}\left[\left(1 + \frac{\varepsilon_{xy,l}}{\varepsilon_{\perp,l}}\right)J_{m-1}(kn_l r_{ls})e^{-i(m-1)\theta_{ls}} - \left(1 - \frac{\varepsilon_{xy,l}}{\varepsilon_{\perp,l}}\right)J_{m+1}(kn_l r_{ls})e^{-i(m+1)\theta_{ls}}\right], \tag{25}$$

while, for the dipole source term H_z^{0y}, the expressions for $\mathbf{K}$ and $\mathbf{Q}$ are given by

$$K_m^l = -\frac{n_b}{8}\left[\left(1 + \frac{\varepsilon_{xy,b}}{\varepsilon_{\perp,b}}\right)H_{m-1}(kn_b r_{ls})e^{-i(m-1)\theta_{ls}} + \left(1 - \frac{\varepsilon_{xy,b}}{\varepsilon_{\perp,b}}\right)H_{m+1}(kn_b r_{ls})e^{-i(m+1)\theta_{ls}}\right], \tag{26}$$

$$Q_m^l = \frac{n_l}{8}\left[\left(1 + \frac{\varepsilon_{xy,l}}{\varepsilon_{\perp,l}}\right)J_{m-1}(kn_l r_{ls})e^{-i(m-1)\theta_{ls}} - \left(1 - \frac{\varepsilon_{xy,l}}{\varepsilon_{\perp,l}}\right)J_{m+1}(kn_l r_{ls})e^{-i(m+1)\theta_{ls}}\right]. \tag{27}$$

Once the linear system has been solved for each of the two source orientations, the magnetic field H_z is reconstructed using global field expansions [Eqs. (20) and (23)]. The components of the electric tensor are calculated using Maxwell's equations.

C. Modes of Gyrotropic Clusters

To find the modes of such clusters, it is necessary to find the null solutions of the homogeneous system in Eq. (16) (without sources):

$$(\mathbf{I} - \mathbf{RH})\mathbf{B} = 0. \tag{28}$$

This requires the vanishing of the determinant of the linear system, i.e.,

$$\det(\mathbf{I} - \mathbf{RH}) = 0. \tag{29}$$

Hence, this is the equivalent of finding the zeroes of the determinant in the complex frequency ω plane or, equivalently, in the complex wavelength plane $\lambda_p = \lambda_p' + i\lambda_p''$. The zeroes are located in the lower half of the complex frequency plane or, equivalently, in the upper half of the complex wavelength plane, because of the causality condition.

The finite cluster is open, and, therefore, all modes are leaky, with their quality factors given by $Q = \lambda_p'/2\lambda_p''$, where λ_p' is the real part of the wavelength and λ_p'' is its imaginary part. The real part λ_p' defines the modal wavelength, while the imaginary part λ_p'' gives its quality factor Q. The modal field can be calculated by the application of singular value decomposition to Eq. (28), which will determine the vector of the multipole coefficients $\mathbf{B}$ for all cylinders. The modal field can then be reconstructed using Eqs. (4) and (9) for TM polarization and Eqs. (20) and (23) for TE polarization, but without the source terms. Other field components are found analytically using Maxwell's equations.

3. METHOD'S CONVERGENCE AND ITS NUMERICAL VERIFICATION

In this section we first provide details of the electromagnetic field convergence studies and verification of the numerical results. The presented multipole method for Green's tensor construction for gyrotropic materials turns out to be as highly efficient and accurate as for the isotropic material case in which ε and μ are scalars [18].

In Table 1, we present the field convergence study for a ferrite cluster composed of $N_c = 25$ of yttrium–iron–garnet

Table 1. Field Convergence Data as a Function of the Retained Multipole Coefficients N_p for TM Polarization (Ferrite Cluster)

$N_p = 2M + 1$	E_z	H_x	H_y
3	−0.0033568320+i0.0013388036	−0.0006632724−i0.0060792630	−0.0009175906+i0.0061410684
5	−0.0032723380+i0.0013442870	−0.0007338791−i0.0060234433	0.0060679854−i0.0009883445
7	−0.0032779380+i0.0013440207	−0.0007261071−i0.0060265626	−0.0009804147+i0.0060428333
9	−0.0032779073+i0.0013440324	−0.0007269206−i0.0060264830	−0.0009812651+i0.0060428056
11	−0.0032779094+i0.0013440326	−0.0007268787−i0.0060264984	−0.0009812215+i0.0060428194
13	−0.0032779095+i0.0013440326	−0.0007268787−i0.0060264985	−0.0009812216+i0.0060428197

cylinders located in air and forming a square lattice with 5×5 sides. The source $\mathbf{c}_s$ is located inside of the central cylinder and has coordinates $(0, 0.001d)$, while the field point position $\mathbf{r}$ has coordinates $(1.5d, 1.5d)$ and is placed in air. The radii of the cylinders are $a = 0.2d$, and $d = 10$ mm is the lattice constant, while the wavelength of the radiation is $\lambda = 3.5d$. The magnetic permeability tensor components [Eq. (1)] have the following forms [21]:

$$\mu_\perp = 1 + \frac{\omega_0 \omega_m}{\omega_0^2 - \omega^2}, \qquad \mu_{xy} = \frac{\omega \omega_m}{\omega_0^2 - \omega^2}, \tag{30}$$

where $\omega_m = 4\pi\gamma M_s$ and $\omega_0 = \gamma H_0$. Here H_0 is the applied external static magnetic field, $4\pi M_s$ is the saturation magnetization, and γ is the gyromagnetic ratio. As in [3], we have used the following values for these parameters: $4\pi M_s = 1750G$, $H_0 = 500Oe$, and dielectric permittivity $\varepsilon = 15$, which are typical parameters for yttrium–iron–garnet ferrites [21].

As Table 1 demonstrates, the field values rapidly converge as the number of retained multipole coefficients $N_p = 2M + 1$ increases (see the first column of the table). For the value of $M = 4$, the field values converge to seven significant figures, which is sufficient for almost all applications, while for $M = 6$, the field value converges to 10 significant figures.

In Table 2 we present a convergence study for a gyroelectric material and the current $\mathbf{j}$ orientation along the x axis. The case of the y orientation of the source is similar and we do not provide this data. The components of the dielectric tensor for gyroelectric background material are $\varepsilon_\perp = 16$ and $\varepsilon_{xy} = 1$, with $\mu = 1$ throughout, while the void cylinders have refractive index $n = 1$. The rest of the parameters are the same as for the convergence study for ferrite cylinders above. The convergence pattern for the gyroelectric cluster is similar to the ferrite cluster. By retaining $M = 4$ multipoles, the field values have at least six converged significant digits, while by keeping $M = 6$, multipoles the field values converge to 10 significant figures.

The boundary conditions on each cylinder are satisfied exactly, facilitating convergence. Such highly accurate results are harder to achieve by using pure numerical methods like finite-difference time-domain (FDTD) [23] or approaches based on the finite element method (FEM) [24]. Although highly accurate results are not necessary for most applications, it is nevertheless important to have a method that can provide such results. There may be some cases where high accuracy is needed and, more generally, our accurate results can be used also for the verification of purely numerical methods.

The generalized Lorentz reciprocity condition [25] $G^e_{\alpha,\beta}(\mathbf{r}, \mathbf{c}_s, \mathbf{H}_0) = G^e_{\beta,\alpha}(\mathbf{c}_s, \mathbf{r}, -\mathbf{H}_0)$ holds with an accuracy of $\sim 10^{-9}$–10^{-10} in the numerical examples. Here $\mathbf{H}_0$ is the external static magnetic field. This is a strict test for the numerical verification of the results, given that the calculations have to be performed with independent routines, e.g., if the source $\mathbf{c}_s$ is located in the background and the field point $\mathbf{r}$ is inside a cylinder, then the reciprocity condition requires us to compare the field value at this point to the field value outside the cylinder $\mathbf{r}$ when the source is located inside the cylinder $\mathbf{c}_s$.

In general, the number of retained multipole coefficients for a given accuracy depends on the wavelength, the radii of the cylinders, and the contrast of the refractive index of cylinders and the background. By simply increasing the number of retained multipole coefficients, any required accuracy can be achieved (within the limits set by a computer and standard function accuracy).

4. CHIRAL HALL EDGE STATE PROPERTIES

In this section we present some important and interesting properties of chiral Hall edge states and their excitations in gyrotropic clusters. First, in Section 4.A we investigate the tolerance of the chiral Hall edge modes of a ferrite cluster toward a cluster split with gap h. Then we report on the evolution of chiral Hall edge states as a function of the split distance h. We also present results of chiral Hall edge mode excitation by a source and their energy flow. Next, in Section 4.B, we consider a gyroelectric cluster and present results of the chiral Hall edge mode excitations for different source orientations.

Table 2. Field Convergence Data as a Function of the Retained Multipole Coefficients N_p for TE Polarization (Gyroelectric Cluster)

$N_p = 2M + 1$	H_z	E_x	E_y
3	−0.1296345389−i0.0426618457	0.0235906111+i0.0053348044	−0.0223966957−i0.0105906933
5	−0.1342563355−i0.0435310832	0.0241285949+i0.0056508534	−0.0023157907−i0.0108383670
7	−0.1339561230−i0.0433692220	0.0240700719+i0.0056030484	−0.0231278238−i0.0108021538
9	−0.1339531835−i0.0433672910	0.0240716603+i0.0056048730	−0.0231257418−i0.0108009142
11	−0.1339533817−i0.0433674547	0.0240716710+i0.0056048832	−0.0231257666−i0.0108009245
13	−0.1339533834−i0.0433674497	0.0240716694+i0.0056048836	−0.0231257688−i0.0108009248

A. Tolerance and Evolution of Chiral Hall Edge Modes in Ferrite Clusters toward Split Degree

Here, we study the tolerance and the transformation of chiral Hall edge modes with respect to a linear split h of a ferrite cluster (see Fig. 2). In this study, we use the cluster parameters and geometry reported in [3], where it was shown that the one-way Hall edge states exist at the edge of a semi-infinite honeycomb ferrite photonic crystal and free space. The parameters of this semi-infinite photonic crystal are the same as for the example used in the convergence test study reported in Table 1, except that the cylinders have formed a honeycomb lattice. It has been shown in [17] that, in such clusters with $N_c = 854$ cylinders, there exists a chiral Hall edge state with wavelength $\lambda/d = 3.928 + i0.0177$ (for details, see Fig. 11 in [17]). Here, we investigate the tolerance and the evolution of these chiral Hall edge states as we introduce a linear separation h in the middle of the cluster (see Fig. 2). Introduction of this cluster separation h splits the initial cluster with $N_c = 854$ cylinders into two clusters with $N_c = 434$ cylinders (left cluster) and $N_c = 420$ (right cluster), creating a waveguide between the clusters. In Fig. 2, we plot the logarithm of the electric field intensity for a chiral Hall edge state with wavelength $\lambda/d = 3.937 + i0.0174$ and with cluster separation $h = 0.25d$. The quality factor of this mode is $Q = 113$. The splitting of the cluster and its separation shifts the chiral Hall edge state wavelength to a slightly higher value. The plot in Fig. 2 demonstrates the remarkable property of the chiral Hall edge mode to withstand a strong separation. The field intensity distribution is still concentrated at the edges of the cluster with little disturbance compared to the cluster without separation. The overall property of the chiral nature of the mode is still retained. This is clearly seen in the plot of the energy flux map in Fig. 3. The Poynting vector flux is largely undisturbed by the cluster separation and reveals the chiral character of the edge mode. Such strong tolerance to separation is based on the topological protection property of chiral Hall edge states.

In Fig. 4 we plot the electric field intensity $|E_z|^2$ for a point source located at $(-7.5d, -6d)$ for the wavelength $\lambda/d = 3.937$, which coincides with the real part of the wavelength of the chiral Hall edge state plotted in Fig. 2. The electromagnetic field excites the chiral Hall edge state and its intensity is confined mainly at the edges of the cluster. Note that the energy flux along the waveguide created by the gap between the clusters is negligible.

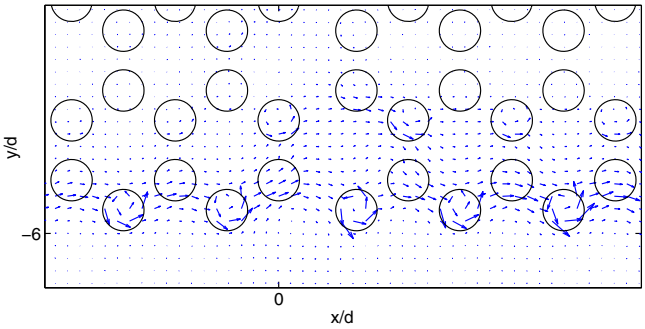

Fig. 3. Poynting vector map for the mode plotted in Fig. 2 showing the energy flow across the separation near $x/d = 0$, $y/d = -6$.

As we increase the gap between the clusters to $h = 0.5d$, we observe that the chiral Hall edge state now has more complicated behavior. The modal field is still concentrated at the outside edges of the whole cluster and circulates anticlockwise, as in Fig. 2, but some energy starts to circulate anticlockwise around the smaller (right) cluster only, while the flux at the right edge of the left cluster is negligible (the plot is not provided).

As we increase the displacement h further, the energy flux at the right-hand edge of the left cluster increases, and at separation $h = 1.96d$ the energy flux of the chiral Hall edge state of the whole cluster is transformed into the chiral Hall edge state of two smaller clusters. At such separations, the energy flux of a chiral Hall edge state circulates anticlockwise around both clusters, and the energy circulation at the gap between the clusters takes place in opposite directions (see Fig. 5).

The intensity distribution of the electric field of this chiral Hall edge mode, which has a quality factor $Q = 151$, is plotted in Fig. 6. The intensity of the field is distributed mainly around the edges of the cluster and within the gap between the clusters. A point source radiating with wavelength $\lambda/d = 3.92$ and located either in the gap between the clusters or close to the edge of one of the clusters will excite this chiral Hall edge state. In contrast to conventional waveguides, the energy flux between the clusters will be directed in opposite directions along the sides of the waveguide walls.

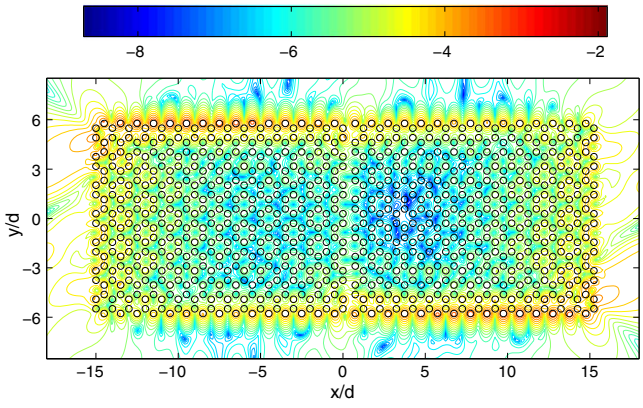

Fig. 2. Logarithm of electric field intensity $|E_z|^2$ of a chiral Hall edge state for a ferrite cluster with a linear split at the center with separation $h = 0.25d$.

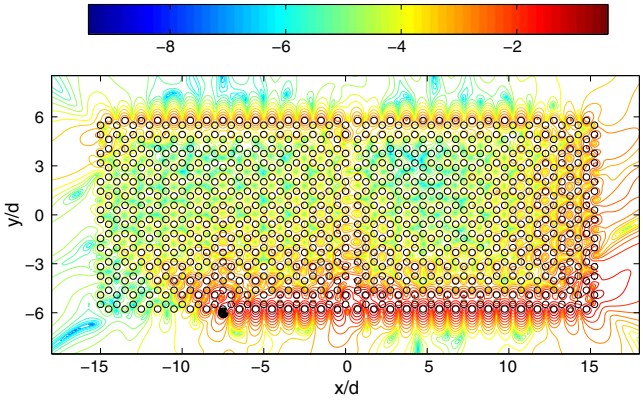

Fig. 4. Intensity of the electric field $|E_z|^2$ with a logarithmic scale excited by a point source indicated by a black dot.

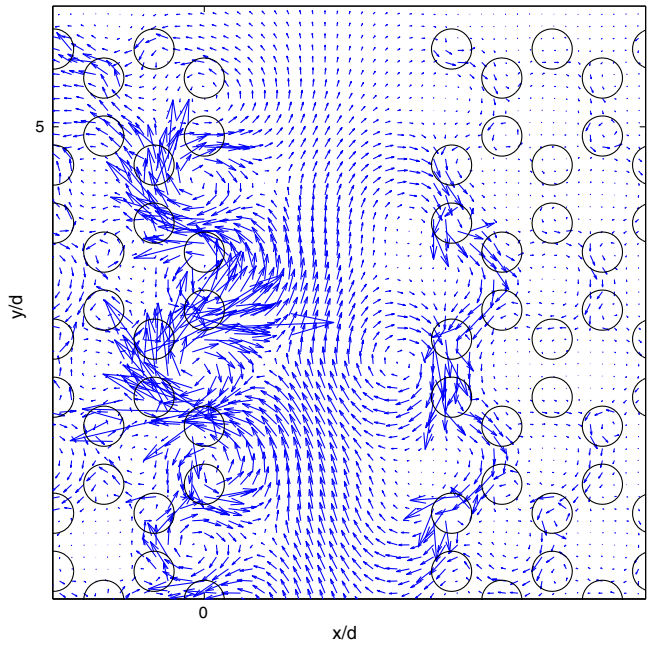

Fig. 5. Poynting vector map of a chiral Hall edge mode with $\lambda/d = 3.92 + i0.013$ for the displacement value $h = 1.96d$ showing the opposite energy flow in the waveguide created by the separation of the clusters.

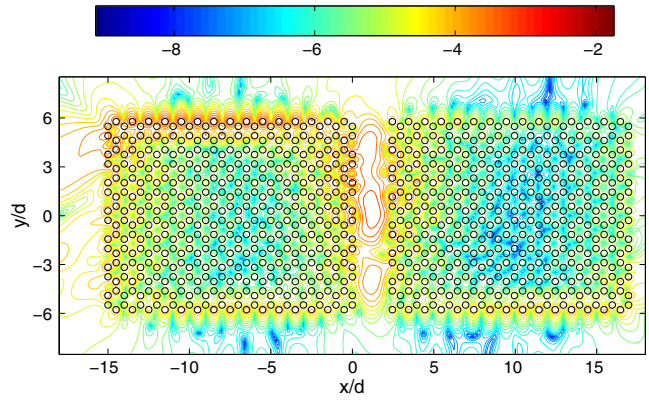

Fig. 6. Logarithm of the electric field intensity $|E_z|^2$ of a chiral Hall edge state with cluster separation $h = 1.96d$.

We also reversed the direction of the external static magnetic field of the right cluster and observed that the energy flux of the chiral Hall edge mode was now directed clockwise for the right cluster and anticlockwise for the left cluster. These unique properties of ferrite clusters can be utilized to construct complex and compact waveguide circuits. The ability to change the direction of the energy flow by changing the direction of the external static magnetic field provides additional means to manipulate the radiation flow.

B. Chiral Hall Edge Mode Excitation in Gyroelectric Clusters

In this subsection, we consider the excitation of chiral Hall edge states for different source orientations in a gyroelectric cluster. As a gyroelectric photonic cluster that exhibits chiral Hall edge states, we use the geometry and parameter set reported in [8]. The geometry of the cluster is plotted in Fig. 7.

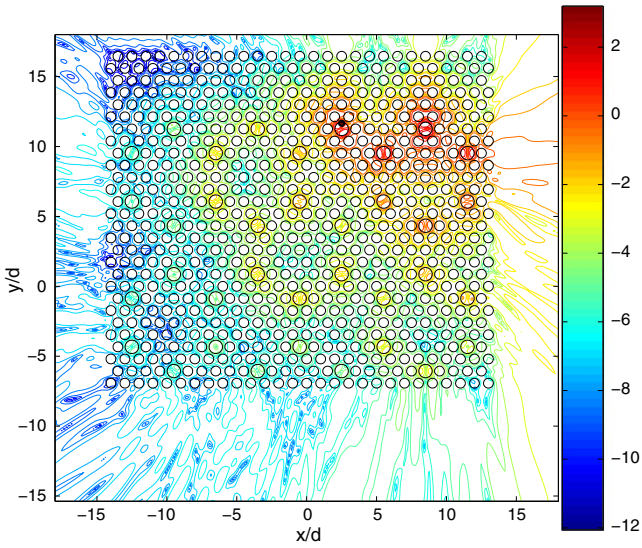

Fig. 7. Intensity of the magnetic field $|H_z|^2$ in the logarithm scale for a source with x-axis orientation. The coordinates of the source are (2.5,11.65), and it is depicted as a black dot.

The photonic cluster has a hexagonal lattice of period d with air cylinders. The cylinders have a radius $a = 0.35d$ and are located in a uniform dielectric with dielectric permittivity $\varepsilon = 16$. In the structure shown in Fig. 7, the top five rows consist of such a photonic cluster. The bottom cluster with 26 rows of cylinders is the same as the top, except that there are gyroelectric cylinders embedded in the hexagonal lattice, which form a honeycomb lattice with period $d' = 6d$ and radii $a = 0.48d$. These are the cylinders with larger radii in Fig. 7. The components of the dielectric tensor for gyroelectric resonators are $\varepsilon_\perp = 16$ and $\varepsilon_{xy} = 1$, while $\mu = 1$ throughout. For more detail, see [8,17]. It has been shown in [17] that there is a chiral Hall edge mode in this cluster with wavelength $\lambda/d = 4.436 + i0.015$ and $Q = 148$. In Fig. 7 we plot the magnetic field distribution for a source oriented in the x direction and located at $(2.5d, 11.65d)$ with $\lambda/d = 4.436$. The source excites the chiral Hall edge mode sandwiched at the interfaces between the upper photonic cluster, which acts as a mirror, and the lower gyroelectric cluster, which breaks time-reversal symmetry and supports one-way radiation along the x direction. This chiral character of the radiation is evident in the field intensity distribution in Fig. 7, where the field is mainly concentrated at the top layer of the gyroelectric cylinders at $y \approx 11d$ and the energy flux is mainly directed to the right from the source.

In Fig. 8, we study the same configuration as in Fig. 7, but for the y orientation of the source. For this orientation of the source, the excited field is concentrated mainly around the six gyroelectric cylinders that form a honeycomb lattice. The energy flux of this field is clockwise. There also exists another pole with $\lambda/d = 4.441 + i0.016$ and $Q = 139$ and the y-oriented source excites this mode of the cluster. This mode is reminiscent of the chiral Hall edge mode for a ferrite hexagonal flake cluster reported in [17] (see Fig. 16 in [17]). Therefore, the mode excitations of the cluster can depend on the source orientation. This is influenced by the proximity of poles to the radiation wavelength and their relatively high quality factors Q. The position of the source can also influence the modal excitation. If the source is located at the nodal point

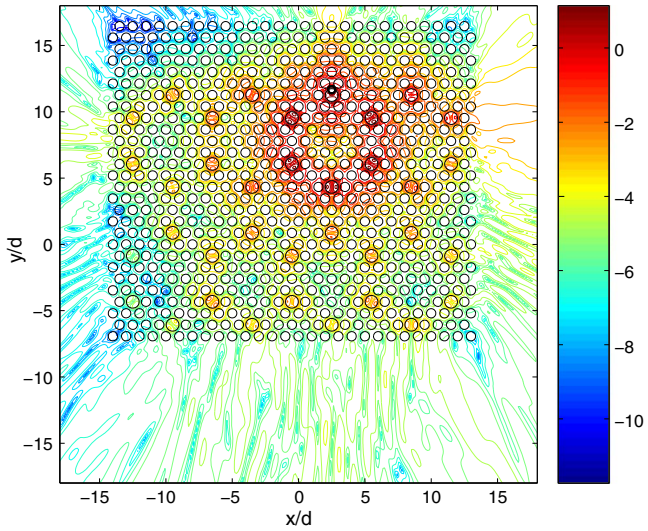

Fig. 8. Same relationship as in Fig. 7 but for a source with y-axis orientation.

of the corresponding mode, then the mode will be hard to excite. The utilization of the unique properties of chiral Hall edge modes requires their excitation, and, therefore, an understanding of their modal excitation is important for practical applications.

5. CONCLUSIONS

The electromagnetic field Green's tensor has been constructed for two-dimensional clusters of gyrotropic cylinders with a circular cross section using the multipole method. The method has been shown to be very accurate and effective. This approach not only calculates the electromagnetic Green's tensor but also finds the electromagnetic modes of such structures and characterizes their energy flow directions. Both ferrites and gyroelectric photonic clusters have been treated. Convergence data has been provided for typical examples to demonstrate the effectiveness of the method. This data can be used as a reference check for purely numerical methods, such as FDTD or FEM.

As an application demonstrating the effectiveness of the method, we have investigated the tolerance and the transformation properties of the chiral Hall edge states in ferrite clusters with respect to the degree of a cluster split with separations h. It is shown that the chiral Hall edge states can withstand substantial cluster separation and preserve their topological structure. Even a large separation value of $h = 0.25d$ does not distort the one-way nature of the chiral Hall edge state. This can be attributed to their topologically protected nature.

The transformation properties of the chiral Hall edge states as a function of the degree of separation h has been investigated, as well. It was established that as the separation h increases, the chiral Hall edge state acquires more complicated behavior. At separation value $h = 0.5d$, the energy flow of the one-way edge state circulates not only around the outside edges of the cluster but acquires additional circulation around one of the smaller clusters. At higher values of h, such as $h = 1.96d$, the chiral Hall edge state energy circulates around the edges of each of the smaller clusters (see Fig. 5). Thus the chiral state behaves as if it is split into two edge states of the separated clusters. Although we did not consider the effects of both separation and rotation of a cluster in respect to another or a linear dislocation of a cluster along a straight line, preliminary calculations indicate that the chiral Hall states can also withstand such kinds of substantial defects.

For both ferrites and gyroelectric clusters, we have studied the excitation of the chiral Hall edge state by a source. For the gyroelectric cluster, we have shown that the excitation of the chiral state can depend on the orientation of the source.

These studies of the properties of chiral Hall edge states are important for their potential applications in future photonic networks. These properties of chiral Hall states can be useful also for electronic systems as photonic edge states are the direct analog of electronic chiral Hall states.

APPENDIX A: INTERFACE REFLECTION AND TRANSMISSION COEFFICIENTS

The interface reflection and transmission coefficients for TM polarization are given by

$$R_m^l = -\frac{J'_m(kn_la_l)J_m(kn_ba_l)/Z_l - J_m(kn_la_l)J'_m(kn_ba_l)/Z_b + \delta_m J_m(kn_la_l)J_m(kn_ba_l)}{J'_m(kn_la_l)H_m^{(1)}(kn_ba_l)/Z_l - J_m(kn_la_l)H_m^{(1)\prime}(kn_ba_l)/Z_b + \delta_m J_m(kn_la_l)H_m^{(1)}(kn_ba_l)}, \tag{A1}$$

$$R_m^{l'} = -\frac{H_m^{(1)\prime}(kn_la_l)H_m^{(1)}(kn_ba_l)/Z_i - H_m^{(1)}(kn_la_l)H_m^{(1)\prime}(kn_ba_l)/Z_b + \delta_m H_m^{(1)}(kn_la_l)H_m^{(1)}(kn_ba_l)}{J'_m(kn_la_l)H_m^{(1)}(kn_ba_l)/Z_l - J_m(kn_la_l)H_m^{(1)\prime}(kn_ba_l)/Z_b + \delta_m J_m(kn_la_l)H_m^{(1)}(kn_ba_l)}, \tag{A2}$$

$$T_m^l = \frac{2\mu_{\perp,l}/(\mu_{\perp,l}^2 - \mu_{xy,l}^2)/(\pi ka_l)}{J'_m(kn_la_l)H_m^{(1)}(kn_ba_l)/Z_l - J_m(kn_la_l)H_m^{(1)\prime}(kn_ba_l)/Z_b + \delta_m J_m(kn_la_l)H_m^{(1)}(kn_ba_l)}, \tag{A3}$$

$$T_m^{l'} = \frac{2\mu_{\perp,b}/(\mu_{\perp,b}^2 - \mu_{xy,b}^2)/(\pi ka_l)}{J'_m(kn_la_l)H_m^{(1)}(kn_ba_l)/Z_l - J_m(kn_la_l)H_m^{(1)\prime}(kn_ba_l)/Z_b + \delta_m J_{m'}(kn_la_l)H_m^{(1)}(kn_ba_l)}, \tag{A4}$$

where Z_l and Z_b are the impedances of the lth cylinder and the background medium, correspondingly given by

$$Z_l = \sqrt{\frac{\mu_{\perp,l}^2 - \mu_{xy,l}^2}{\varepsilon_l \mu_{\perp,l}}}, \qquad Z_b = \sqrt{\frac{\mu_{\perp,b}^2 - \mu_{xy,b}^2}{\varepsilon_b \mu_{\perp,b}}}, \qquad \delta_m = \frac{m}{ka_l}\left(\frac{\mu_{xy,l}}{\mu_{\perp,l}^2 - \mu_{xy,l}^2} - \frac{\mu_{xy,b}}{\mu_{\perp,b}^2 - \mu_{xy,b}^2}\right). \tag{A5}$$

The interface reflection and transmission coefficients for TE polarization are given by the relations

$$R_m^l = -\frac{J_m'(kn_la_l)J_m(kn_ba_l)Z_l - J_m(kn_la_l)J_m'(kn_ba_l)Z_b + \delta_m J_m(kn_la_l)J_m(kn_ba_l)}{J_m'(kn_la_l)H_m^{(1)}(kn_ba_l)Z_l - J_m(kn_la_l)H_m^{(1)\prime}(kn_ba_l)Z_b + \delta_m J_m(kn_la_l)H_m^{(1)}(kn_ba_l)}, \tag{A6}$$

$$R_m^{l'} = -\frac{H_m^{(1)\prime}(kn_la_l)H_m^{(1)}(kn_ba_l)Z_i - H_m^{(1)}(kn_la_l)H_m^{(1)\prime}(kn_ba_l)Z_b + \delta_m H_m^{(1)}(kn_la_l)H_m^{(1)}(kn_ba_l)}{J_m'(kn_la_l)H_m^{(1)}(kn_ba_l)Z_l - J_m(kn_la_l)H_m^{(1)\prime}(kn_ba_l)Z_b + \delta_m J_m(kn_la_l)H_m^{(1)}(kn_ba_l)}, \tag{A7}$$

$$T_m^l = \frac{2\varepsilon_{\perp,l}/(\varepsilon_{\perp,l}^2 - \varepsilon_{xy,l}^2)/(\pi k a_l)}{J_m'(kn_la_l)H_m^{(1)}(kn_ba_l)Z_l - J_m(kn_la_l)H_m^{(1)\prime}(kn_ba_l)Z_b + \delta_m J_m(kn_la_l)H_m^{(1)}(kn_ba_l)}, \tag{A8}$$

$$T_m^{l'} = \frac{2\varepsilon_{\perp,b}/(\varepsilon_{\perp,b}^2 - \varepsilon_{xy,b}^2)/(\pi k a_l)}{J_m'(kn_la_l)H_m^{(1)}(kn_ba_l)Z_l - J_m(kn_la_l)H_m^{(1)\prime}(kn_ba_l)Z_b + \delta_m J_m'(kn_la_l)H_m^{(1)}(kn_ba_l)}, \tag{A9}$$

where

$$Z_l = \sqrt{\frac{\varepsilon_{\perp,l}^2 - \varepsilon_{xy,l}^2}{\mu_l \varepsilon_{\perp,l}}}, \qquad Z_b = \sqrt{\frac{\varepsilon_{\perp,b}^2 - \varepsilon_{xy,b}^2}{\mu_b \varepsilon_{\perp,b}}}, \qquad \delta_m = \frac{m}{ka_l}\left(\frac{\varepsilon_{xy,l}}{\varepsilon_{\perp,l}^2 - \varepsilon_{xy,l}^2} - \frac{\varepsilon_{xy,b}}{\varepsilon_{\perp,b}^2 - \varepsilon_{xy,b}^2}\right). \tag{A10}$$

ACKNOWLEDGMENTS

Kejie Fang and Shanhui Fan acknowledge support from the U.S. Air Force Office of Scientific Research (grant no. FA9550-09-1-0704) and the U.S. National Science Foundation (grant no. ECCS-1201914). The computational resources used in this work were provided by Intersect Ltd. This research was supported by the Australian Research Council Centre of Excellence for Ultrahigh Bandwidth Devices for Optical Systems (project number CE110001018).

REFERENCES

1. Z. Wang, Y. D. Chong, J. D. Joannopoulos, and M. Soljacic, "Reflection-free one-way edge modes in a gyromagnetic photonic crystal," Phys. Rev. Lett. **100**, 013905 (2008).
2. Z. Wang, Y. D. Chong, J. D. Joannopoulos, and M. Soljacic, "Observation of unidirectional backscattering-immune topological electromagnetic states," Nature **461**, 772–775 (2009).
3. X. Ao, Z. Lin, and C. T. Chan, "One-way edge mode in a magneto-optical honeycomb photonic crystal," Phys. Rev. B **80**, 033105 (2009).
4. Z. Yu, G. Veronis, Z. Wang, and S. Fan, "One-way electromagnetic waveguide formed at the interface between a plasmonic metal under a static magnetic field and a photonic crystal," Phys. Rev. Lett. **100**, 023902 (2008).
5. T. Ochiai and M. Onoda, "Photonic analog of graphene model and its extension: Dirac cone, symmetry, and edge states," Phys. Rev. B **80**, 155103 (2009).
6. Y. Hadad, Y. Mazor, and B. Z. Steinberg, "Green's function theory for one-way particle chains," Phys. Rev. B **87**, 035130 (2013).
7. H. Zhu and C. Jiang, "Broadband unidirectional electromagnetic mode at interface of anti-parallel magnetized media," Opt. Express **18**, 6914–6921 (2010).
8. K. Fang, Z. Yu, and S. Fan, "Microscopic theory of photonic one-way edge mode," Phys. Rev. B **84**, 075477 (2011).
9. F. D. M. Haldane and S. Raghu, "Possible realization of directional optical waveguides in photonic crystals with broken time-reversed symmetry," Phys. Rev. Lett. **100**, 013904 (2008).
10. S. Raghu and F. D. M. Haldane, "Analogs of quantum-Hall-effect edge states in photonic crystals," Phys. Rev. A **78**, 033834 (2008).
11. F. D. M. Haldane, "Model for a quantum Hall effect without Landau levels: condensed-matter realization of the 'parity anomaly'," Phys. Rev. Lett. **61**, 2015–2018 (1988).
12. D. J. Thouless, M. Kohmoto, M. P. Nightingale, and M. den Nijs, "Quantized Hall conductance in a two-dimensional periodic potential," Phys. Rev. Lett. **49**, 405–408 (1982).
13. M. L. Povinelli, S. G. Johnson, E. Lidorikis, J. D. Joannopoulos, and M. Soljačić, "Effects of a photonic band gap on scattering from waveguide disorder," Appl. Phys. Lett. **84**, 3639–3641 (2004).
14. T. N. Langtry, A. A. Asatryan, L. C. Botten, C. M. de Sterke, R. C. McPhedran, and P. A. Robinson, "Effects of disorder in two-dimensional photonic crystal waveguides," Phys. Rev. E **68**, 026611 (2003).
15. R. Balian and C. Bloch, "Distribution of eigenfrequencies for the wave equation in a finite domain. II. Electromagnetic field. Riemannian spaces," Ann. Phys. **64**, 271–307 (1971).
16. E. N. Economou, *Green's Functions in Quantum Physics* (Springer-Verlag, 2006).
17. A. A. Asatryan, L. C. Botten, K. Fang, S. Fan, and R. C. McPhedran, "Local density of states of chiral Hall edge states in gyrotropic photonic clusters," Phys. Rev. B **88**, 035127 (2013).

18. A. A. Asatryan, K. Busch, R. C. McPhedran, L. C. Botten, C. M. de Sterke, and N. A. Nicorovici, "Two-dimensional Green tensor and local density of states in finite-sized two-dimensional photonic crystals," Waves Random Media **13**, 9–25 (2003).
19. A. A. Asatryan, K. Busch, R. C. McPhedran, L. C. Botten, C. M. de Sterke, and N. A. Nicorovici, "Two-dimensional Green's function and local density of states in photonic crystals consisting of a finite number of cylinders of infinite length," Phys. Rev. E **63**, 046612 (2001).
20. A. A. Asatryan, S. Fabre, K. Busch, R. C. McPhedran, L. C. Botten, C. M. de Sterke, and N. A. Nicorovici, "Two-dimensional local density of states in two-dimensional photonic crystals," Opt. Express **8**, 191–196 (2001).
21. D. M. Pozar, *Microwave Engineering* (Wiley, 1988).
22. W. C. Chew, *Waves and Fields in Inhomogeneous Media* (IEEE, 1995).
23. A. Taflove and S. C. Hagness, *Computational Electrodynamics: The Finite-Difference Time-Domain Method* (Artech House, 2005).
24. J.-M. Jin, *The Finite Element Method in Electromagnetics* (Wiley, 2002).
25. J. A. Kong, *Electromagnetic Wave Theory* (EMW Publishing, 2005).